doi: 10.29382/eqs-2020-0161-01

Stress drop assessment of the August 8, 2017, Jiuzhaigou earthquake sequence and its tectonic implications*

Xi He[1] Lian-Feng Zhao[1,✉] Xiao-Bi Xie[2] Lin Shen[2] Wei-Min Wang[3]
Zhen-Xing Yao[1]

[1] *Key Laboratory of Earth and Planetary Physics*, *Institute of Geology and Geophysics*, *Chinese Academy of Sciences*, *Beijing* 100029, *China*
[2] *Institute of Geophysics and Planetary Physics*, *University of California at Santa Cruz*, *CA* 95064, *USA*
[3] *Key Laboratory of Continental Collision and Plateau Uplift*, *Institute of Tibetan Plateau Research*, *Chinese Academy of Sciences*, *Beijing* 100101, *China*

Abstract By using a broadband Lg attenuation model developed for the Tibetan Plateau, we isolate source terms by removing attenuation and site effects from the observed Lg-wave displacement spectra of the M 7.0 earthquake that occurred on August 8, 2017, in Jiuzhaigou, China, and its aftershock sequence. Thus, the source parameters, including the scalar seismic moment, corner frequency and stress drop, of these events can be further estimated. The estimated stress drops vary from 47.1 kPa to 7149.6 kPa, with a median value of 59.4 kPa and most values falling between 50 kPa and 75 kPa. The estimated stress drops show significant spatial variations. Lower stress drops were mainly found close to the mainshock and on the seismogenic fault plane with large coseismic slip. In contrast, the highest stress drop was 7.1 MPa for the mainshock, and relatively large stress drops were also found for aftershocks away from the major seismogenic fault and at depths deeper than the zone with large coseismic slip. By using a statistical method, we found self-similarity among some of the aftershocks with a nearly constant stress drop. In contrast, the stress drop increased with the seismic moment for other aftershocks. The amount of stress released during earthquakes is a fundamental characteristic of the earthquake rupture process. As such, the stress drop represents a key parameter for improving our understanding of earthquake source physics.

Keywords: scalar seismic moment; corner frequency; stress drop; Lg attenuation; Jiuzhaigou earthquake

1 Introduction

On August 8, 2017, a devastating earthquake occurred in the Jiuzhaigou scenic region in Sichuan Province, China, causing 25 fatalities, 525 injuries and 6 missing people (http://www.xinhuanet.com/politics/szzsyzt/scjzgdz170808/index.htm). As reported by the China Earthquake Network Center (CENC), the magnitude 7.0 Jiuzhaigou earthquake occurred at 21:49:24 local time (13:19:46 UTC) and was located at 103.82°E, 33.20°N with a depth of 20 km (Figure 1). Waveform inversions indicated that the seismic moment magnitude M_W was approximately 6.5, and the focal mechanism solutions indicated dominantly strike-slip faulting (Han et al., 2018; Liang et al., 2018b; Yang et al., 2017; Yi et al., 2017). The results published by different authors were comparable, despite slight differences (Table 1). Based on coseismic slip models inverted from geodetic observations, the rupture process of the Jiuzhaigou earthquake was dominated by a left-lateral slip with a deficit of shallow slip (Chen et al., 2018; Ji et al., 2017; Shan et al., 2017; Sun et al., 2018; Wang et al., 2018). The epicentral region features complicated and intricate fault systems, which are mainly composed of the Kunlun, Tazang, Huya and Minjiang faults (Figure 1a). However, the main seismogenic fault of the Jiuzhaigou earthquake is not directly linked to any of these faults, and a field survey failed to identify any surface ruptures or the seismogenic fault itself (Xu et al., 2017b). Aftershock relocation demonstrated that the aftershocks were confined within a narrow zone that extended from the epicenter of the mainshock both northwest toward the juncture of the Tazang and Minjiang faults and southeast to the northern end of the Huya fault (Fang et al., 2018; Liang et al., 2018a; Liang et al., 2018b;

---

* **Received** 15 March 2020; **accepted in revised form** 9 October 2020; **published** 12 December 2020.

✉ **Corresponding author. e-mail**: zhaolf@mail.iggcas.ac.cn

Yi et al., 2017). The distribution of aftershocks outlined a near-vertical and south-southeast-trending fault plane coinciding with one of the nodal planes of the focal mechanism solutions for the mainshock (Han et al., 2018; Liang et al., 2018b; Yang et al., 2017; Yi et al., 2017). The morphology and kinetics of this seismogenic fault were consistent with the south-southeast strike and sinistral nature of the Huya strike-slip fault, indicating that the Jiuzhaigou earthquake might have occurred on a young fault representing a blind extension of the Huya fault (e.g., Sun et al., 2018; Yang et al., 2017; Yi et al., 2017).

The 2017 Jiuzhaigou earthquake, with a magnitude of 7.0, was the third largest earthquake on the eastern margin of the Bayan Har block since the 2008 Wenchuan M_S 8.0 and 2010 Lushan M_S 7.0 earthquakes. The Bayan Har block is one of the major components involved in the eastward expansion of the Tibetan Plateau, and its eastward movement is accommodated by significant (~10–12 mm/a) sinistral slip along its northern boundary, the Kunlun fault (Zhang et al., 2004). The slip rate on the

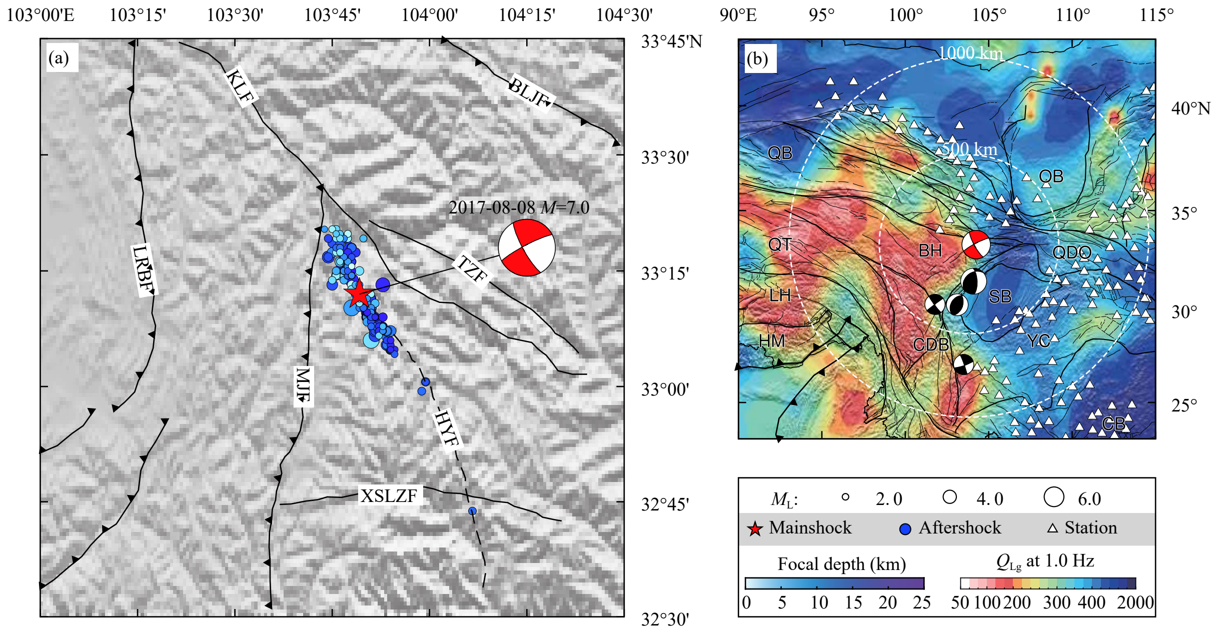

Figure 1 Maps of (a) the August 8, 2017, Jiuzhaigou M_L 7.0 earthquake (red star) and its sequence (filled circles), and (b) seismic Lg-wave Q distribution at 1.0 Hz (Zhao et al., 2013), overlaid on the locations of faults and sutures (black lines) and stations (triangles), with the relevant legend. The focal mechanisms of the Jiuzhaigou earthquake (red) and nearby large earthquakes (black) were retrieved from GCMT (http://www.globalcmt.org), the smaller aftershocks (circles) are plotted according to their magnitudes and depths, respectively. The abbreviations are as follows: BLJF is Bailongjiang fault; HYF is Huya fault; LRBF is Longriba fault; KLF is Kunlun fault; MJF is Minjiang fault; TZF is Tazang fault; XSLZF is Xueshanliangzi fault; HM is Himalaya; LH is Lhasa; QT is Qiangtang; QB is Qaidam basin; BH is Bayan Har block; OB is Ordos basin; QDO is Qingling-Dabie orogeny; SB is Sichuan basin; YC is Yangtze craton; CDB is Chuandian block; CB is Cathaysia block

Table 1 Comparison of the global centroid solutions of focal mechanism for the 2017 Jiuzhaigou earthquake from different authors

Reference	M_W	Centroid location			Nodal plane 1			Nodal plane 2		
		Longitude (°E)	Latitude (°N)	Depth (km)	Strike (°)	Dip (°)	Rake (°)	Strike (°)	Dip (°)	Rake (°)
NEIC	6.51	103.855	33.193	13.5	153	84	–33	246	57	–173
GCMT	6.5	103.89	33.21	16.2	151	79	–8	243	82	–168
Liang et al., 2018	6.5	103.89	33.21	15.5	155.7	87.1	–6.3	246	83.7	–177
Han et al., 2018	6.5	–	–	14	150	78	–13	242	77	–168
Yi et al., 2017	6.4	103.8167	33.1954	5	156	79	–9	248	81	–169
Yang et al., 2017	6.36	103.83	33.22	22	150	80	–20	244	70	–169

Kunlun fault was found to decrease toward the east and was partially absorbed by deformation surrounding the fault tip (Kirby et al., 2007). The left-lateral motion is also transferred to the horsetail-shaped splay faults associated with the Kunlun fault, including the Tazang, Huya and Minjiang faults (Xu et al., 2017b). Subsurface crust images from P-wave receiver functions suggest that these processes may result in a massive thrust nappe structure beneath the Minjiang fault and in the uplift of this region (Liu et al., 2017). The intense crustal deformation and complicated fault system produce intense seismic activity on the eastern margin of the Bayan Har block. In particular, the Jiuzhaigou region was located in a historical earthquake gap and has been identified as an area at risk for potentially large earthquakes (Xu et al., 2017a).

Previous investigations of the 2017 Jiuzhaigou earthquake have provided information on the mainshock and have shed light on the regional tectonic setting as well. Defined as the difference between average stresses on a fault before and after an earthquake, the stress drop $\Delta\sigma$ is one of the fundamental source-scaling parameters used to characterize an earthquake, and it provides information on the physics of the rupture processes and exhibits regional variation related to the tectonic setting (Abercrombie and Rice, 2005; Allmann and Shearer, 2009; Shearer, 2009; Shearer et al., 2006). Given the priori assumptions made in the source model (e.g., Brune, 1970), estimating the stress drop is not easy because it is closely related to the shape of the source spectrum, which can be distorted by seismic attenuation, especially at higher frequencies. To retrieve the source spectrum from the observed spectrum of a large earthquake, the empirical Green's function (EGF) method takes the spectra of nearby small earthquakes, which have sufficiently high corner frequencies and are flat over the observation band, as an approximation of Earth's response to a delta-function source and can then correct the spectrum of the target event for attenuation and other path effects (e.g., Allmann and Shearer, 2009; Shearer et al., 2006). However, the EGF method requires small earthquakes close enough to the target one and cannot remove the effects of near-source attenuation that may vary across regions. Another approach for large datasets in which an event is recorded by multiple stations is to directly solve for the attenuation term using generalized inversion methods and then to compensate the spectrum using the calculated attenuation (e.g., Oth, 2013; Oth et al., 2011). However, this approach can result in difficulties due to the trade-off between the source and attenuation terms. The eastern Tibetan Plateau is characterized by strong attenuations with significant lateral variations. Therefore, a reliable high-resolution broadband attenuation model could greatly improve the accuracy of the stress drop measurements for the Jiuzhaigou earthquake and its aftershocks.

In this paper, based on corrections using a regional Lg-wave Q model covering the eastern Tibetan Plateau with a resolution of approximately 1 degree and a broad frequency band from 0.05 Hz to 10.0 Hz (Zhao et al., 2013a, 2013b), we obtained the Lg-wave source spectra for the 2017 Jiuzhaigou earthquake and its aftershock sequence. Adopting the Brune (1970) source model, we estimated the seismic moments and corner frequencies and calculated the regional average stress drop for the Jiuzhaigou area. The temporal and spatial variations in the stress drop were investigated, improving the understanding of seismic energy release during the Jiuzhaigou earthquake. Because source spectra were retrieved independently at individual frequencies without prior assumptions, such as the constant stress drop model, which leads to conclusions of self-similar source physics, we were able to investigate the self-similarity of the Jiuzhaigou earthquake sequence, which could provide hints regarding the tectonic background and physical mechanism of these earthquakes.

2 Data and methods

The 2017 Jiuzhaigou earthquake and its aftershock sequence generated abundant seismograms recorded by broadband digital seismic stations at regional distances. Based on the CENC catalog, 194 aftershocks occurring before 6 October 2017 with magnitudes greater than 2.0 were selected, and their origin times, epicenters and depths were obtained from the catalog. We collected seismic data from 166 CENC stations from the China National Digital Seismic Network (CNDSN) to investigate the source spectra for the 2017 Jiuzhaigou earthquake and its aftershocks.

To model the source spectra using Lg waveforms, we followed the method used by Zhao and his coworkers (Zhao and Xie, 2016; Zhao et al., 2010, 2013a; Zhao et al., 2013b). First, the Lg waveforms were extracted using a group velocity window of 3.6–3.0 km/s, and a time window with the same length was used before the first P-wave arrival to pick the pre-event noise. Spectra for both Lg-wave and noise were calculated and sampled at 58 individual frequencies log-evenly distributed between 0.05 Hz and 10.0 Hz. Next, we calculated the signal-to-noise ratios at individual frequencies and dropped out low-quality data with a signal-to-noise ratio less than 2.0. Last, by conducting the noise correction, $A_{\mathrm{S}}^2(f) = A_{\mathrm{O}}^2(f) - A_{\mathrm{N}}^2(f)$, where $A(f)$ is the spectral amplitude and the subscripts S, O and N denote the true signal, the observations from the raw Lg waveforms, and the noise series, respectively.

For the observation of event k at station i, the Lg-wave spectral amplitudes A_{ki} can be written in the following form

$$A_{ki} = S_k G_{ki} \Gamma_{ki} P_i R_{ki}, \tag{1}$$

where S is the source term, G is the geometrical spreading factor, Γ_{ki} is the attenuation term that can be expressed by an integral along a great circle ray path from event k to station i, P is the site response term and R is the computational error and cumulative random effects in the Lg propagation between station i and event k. The geometrical spreading is $G_{ki} = (\Delta_0 \Delta_{ki})^{-1/2}$, with Δ_{ki} representing the epicentral distance from event k to station i and Δ_0 representing a reference distance fixed at 100 km. In this study, the path attenuation Γ_{ki} was computed using a regional Lg-wave attenuation model (Zhao et al., 2013b). This Lg-wave attenuation model was derived using tomography based on the single-station and two-station Lg amplitude, and the inversion was done at individual frequencies independently without any assumptions on frequency dependence. Strong lateral variations correlated to the geological structures and tectonics were revealed in this attenuation model, which provided useful information on the deformation of the crust in the Tibetan Plateau. According to formulas from Zhao et al. (2010), the path attenuation from an event to a station can be directly calculated given an Lg-wave Q model. Therefore, with known attenuation and geometric spreading terms, we can strip the propagation effects from the raw Lg-wave spectra A_{ki} from individual stations. Then, by fitting spectra from multiple stations with the theoretical source model using the least-squares orthogonal factor decomposition method (LSQR, Paige and Saunders, 1982), we obtained the source spectrum S. In practice, to take site effects into account, we allowed small perturbations in the attenuation to deal with the trade-off between attenuation and site terms, and we treated the site response as unresolved error. In this way, we hope to reduce potential effects from uncertainty in site response. In addition, the majority of the stations used in this study are located off the Tibetan Plateau, and these stations are generally located in surrounding high-Q regions and have similar tectonic backgrounds. Consequently, the site response probably varies little among these stations. However, a simplified assumption regarding site effects could still limit the reliability of our measurements.

3 Results

3.1 Seismic moment and source spectrum corner frequency

By removing attenuation effects from the raw spectra using the high-resolution broadband Lg-wave Q model, we obtained the Lg-wave source spectral amplitudes at 58 discrete frequencies for the 2017 Jiuzhaigou earthquake and its 166 aftershocks. For these source spectra, their high-frequency amplitudes fell off at a slope of approximately –2 on the log-log scale. Therefore, the commonly used ω^{-2} source model (Brune, 1970) could provide a good fit to Lg-wave spectral data from the Jiuzhaigou earthquake sequence. Based on the theoretical model, the source spectrum can be written as

$$S(f) = \frac{M_0}{4\pi\rho v^3 \left[1 + (f/f_{\mathrm{c}})^2\right]}, \tag{2}$$

where M_0 is the seismic moment, f_{c} is the corner frequency and ρ and v are the average density and shear wave velocity in the source region (Herrmann and Kijko, 1983; Street et al., 1975). A typical value of 2.7 kg/m^3 was assigned to the density ρ, and the shear wave velocity $v = 3.3$ km/s was obtained from Bao et al. (2015). M_0 and f_{c} can then be determined by minimizing the L2 norm of the residuals between the theoretical source function and the network-determined source spectral data. The bootstrap method (Efron, 1983) was used to provide the standard deviation of the two parameters. Examples of the inverted source spectral amplitudes and the best-fit source functions for selected events are shown in Figure 2, and the inverted M_0 and f_{c} for all events are listed in Table 2. The seismic moment and corner frequency for the 2017 mainshock were $(9.88 \pm 2.13) \times 10^{17}$ N·m and 0.18 ± 0.03 Hz. For aftershocks with local magnitudes between 2.0 and 4.9, the seismic moments and corner frequencies ranged from 2.06×10^{17} N·m to 6.34×10^{13} N·m and from 0.95 Hz to 0.062 Hz, respectively. Based on the linear regression, the relationship between the magnitude M_{L} and seismic moment M_0 is $\log_{10} M_0 = 0.42 M_{\mathrm{L}} + 13.78$ (Figure 3).

3.2 Stress drop

For a circular fault, the stress drop is given by

$$\Delta\sigma = \frac{7M_0}{16}\left(\frac{1}{r}\right)^3, \tag{3}$$

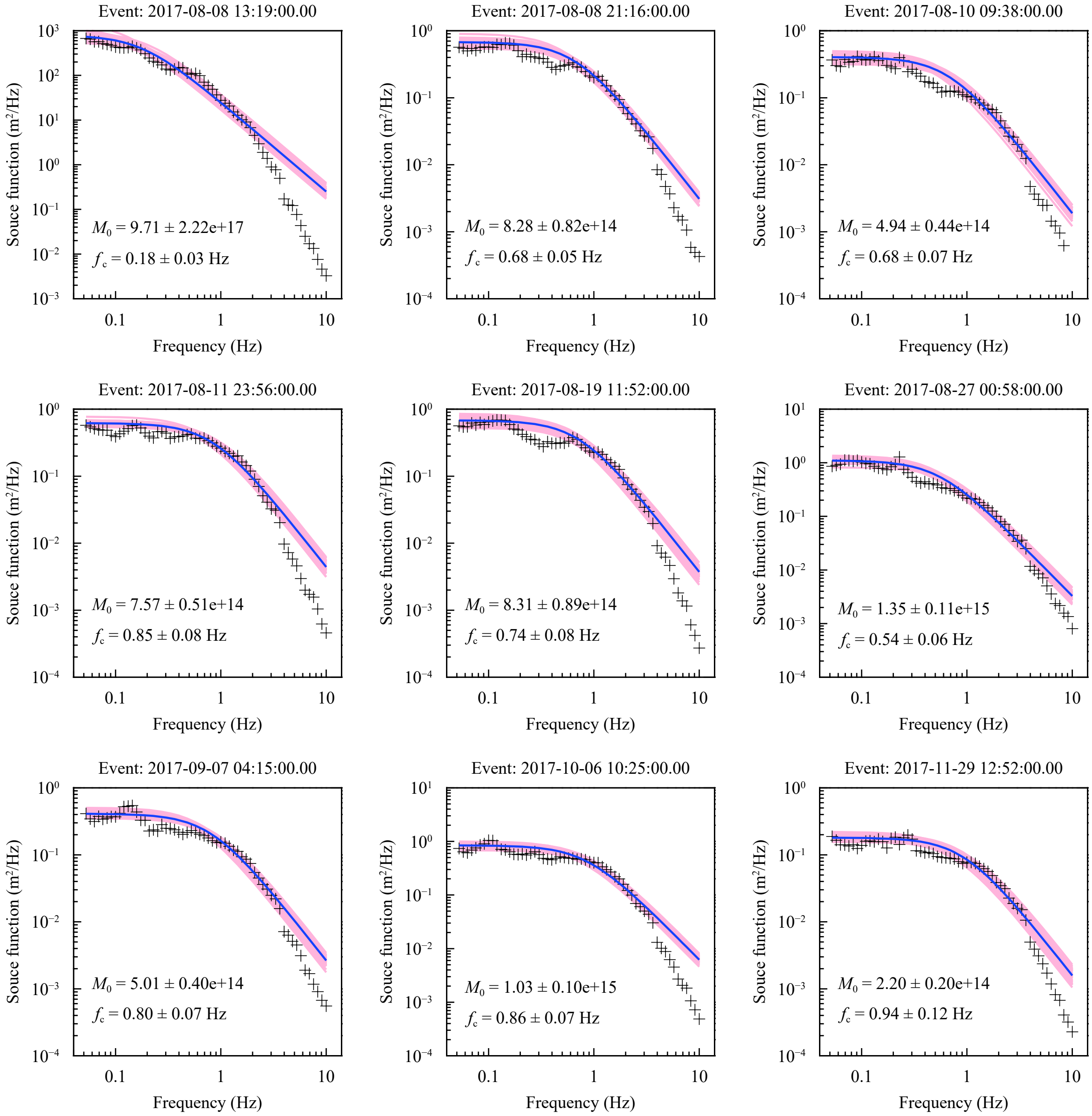

Figure 2 Retrieved Lg-wave source excitation spectra for the August 8, 2017, Jiuzhaigou earthquake and selected aftershocks. Crosses are directly inverted source functions from observed Lg spectra after correction for the propagation effect. Blue solid lines are best-fitting ω^{-2} source models, and pink shaded areas are the standard deviations. The resulting M_0 and f_c values are labeled with their standard errors in each plot

where r is the radius of the fault (Eshelby and Peierls, 1957) and can be expressed as

$$r = \frac{kv}{f_c}, \tag{4}$$

where f_c is the observed corner frequency, v is the shear wave velocity in the source region and k is a constant depending on the specific theoretical source model. Assuming the rupture velocity to be 0.9v, Madariaga (1976) performed finite differences calculations and found that k is 0.21 for S-waves and 0.32 for P-waves given an ω^{-2} high-frequency falloff rate. Combining equations (3)–(4), the Brune-type stress drop can be estimated from the best-fit seismic moment and corner frequency using

$$\Delta\sigma = \frac{7M_0}{16}\left(\frac{f_c}{0.21v}\right)^3. \tag{5}$$

The stress drops calculated from spectral data obtained for the Jiuzhaigou earthquake sequence by using equation (5) showed large variations from 47.1 kPa for a low stress drop aftershock to 7.1 MPa for the mainshock. The median value of the stress drop was 59.4 kPa, and most values were between 50 kPa and 75 kPa. The 7.1 MPa stress drop for the mainshock was close to the 6.0 MPa median value

Table 2 Earthquake parameters used in this study

Epicentral parameters					M_L	Number of recording stations	Inverted source parameters		
Data (a-mo-d)	Time (UTC)	Latitude (°N)	Longitude (°E)	Depth (km)			Seismic moment M_0 (N·m)	Corner frequency f_c (Hz)	Stress drop $\Delta\sigma$ (kPa)
2017-08-08	13:19:0.0000	33.2000	103.8200	10.0	7.0	149	9.71±2.22e+17	0.18±0.03	7149.6±3896.7
2017-08-08	13:27:0.0000	33.1900	103.8500	8.0	2.9	5	1.18±0.47e+17	0.08±0.02	70.2±53.5
2017-08-08	13:34:0.0000	33.2500	103.8200	5.0	2.7	5	2.97±0.79e+16	0.12±0.01	59.6±27.0
2017-08-08	13:41:0.0000	33.1700	103.8400	13.0	3.3	90	3.43±2.30e+16	0.10±0.02	48.4±40.0
2017-08-08	13:42:0.0000	33.1300	103.8800	17.0	2.3	71	2.33±0.96e+16	0.12±0.02	48.5±28.8
2017-08-08	13:51:0.0000	33.2400	103.7900	6.0	2.3	5	2.50±2.02e+16	0.12±0.03	53.9±56.9
2017-08-08	14:0:0.0000	33.0100	103.9900	11.0	2.6	35	1.79±1.03e+15	0.28±0.05	53.5±43.1
2017-08-08	14:1:0.0000	33.2600	103.7900	11.0	2.2	14	3.48±1.56e+14	0.55±0.11	77.3±57.6
2017-08-08	14:6:0.0000	33.2000	103.8300	3.0	2.2	7	3.73±8.04e+14	0.49±0.13	57.3±131.6
2017-08-08	14:13:0.0000	33.2700	103.8000	17.0	2.5	12	2.07±3.96e+16	0.13±0.05	54.8±125.6
2017-08-08	14:19:0.0000	33.2000	103.8200	2.0	2.1	25	2.58±2.64e+14	0.56±0.18	59.9±85.1
2017-08-08	14:20:0.0000	33.1900	103.8200	7.0	2.1	37	6.26±7.85e+14	0.40±0.13	53.5±84.9
2017-08-08	15:0:0.0000	33.1800	103.8200	4.0	2.1	7	8.97±10.00e+16	0.08±0.03	60.1±93.1
2017-08-08	15:4:0.0000	33.2600	103.7900	14.0	3.0	74	1.00±0.42e+15	0.34±0.06	53.3±34.0
2017-08-08	15:6:0.0000	33.2900	103.7600	3.0	2.2	22	2.25±0.87e+15	0.27±0.04	60.5±36.7
2017-08-08	15:7:0.0000	33.2400	103.7600	3.0	2.5	4	2.95±0.50e+15	0.24±0.02	54.8±17.5
2017-08-08	15:22:0.0000	33.2500	103.7600	9.0	2.4	23	9.97±3.39e+14	0.33±0.04	48.6±24.2
2017-08-08	15:25:0.0000	33.2500	103.7800	19.0	2.5	8	3.88±1.09e+15	0.22±0.02	52.2±22.5
2017-08-08	15:26:0.0000	33.1900	103.8500	17.0	2.6	39	3.53±0.91e+14	0.52±0.08	65.8±33.2
2017-08-08	15:30:0.0000	33.2500	103.8000	24.0	2.5	19	3.65±1.19e+14	0.48±0.07	54.1±30.2
2017-08-08	15:35:0.0000	33.2600	103.7900	13.0	2.4	41	2.94±1.37e+14	0.54±0.08	59.4±38.7
2017-08-08	15:46:0.0000	33.2900	103.7900	19.0	2.4	46	2.89±0.67e+14	0.52±0.05	53.7±21.0
2017-08-08	15:49:0.0000	33.2800	103.7800	19.0	3.0	89	7.41±1.87e+14	0.55±0.08	158.2±83.6
2017-08-08	15:51:0.0000	33.1200	103.8900	12.0	3.2	41	7.44±2.13e+14	0.60±0.13	215.4±147.8
2017-08-08	15:54:0.0000	33.2300	103.7800	9.0	2.4	9	2.06±0.61e+17	0.06±0.01	62.7±34.3
2017-08-08	16:5:0.0000	33.1800	103.8600	8.0	2.5	72	4.13±0.63e+14	0.51±0.06	71.8±26.9
2017-08-08	16:19:0.0000	33.2000	103.8200	15.0	2.2	35	1.28±0.52e+14	0.67±0.09	50.1±29.1
2017-08-08	16:29:0.0000	33.2900	103.7700	4.0	2.1	27	1.08±0.35e+14	0.74±0.09	56.6±27.7
2017-08-08	16:30:0.0000	33.2000	103.8500	3.0	2.1	5	1.31±0.55e+16	0.31±0.12	525.9±644.6
2017-08-08	16:35:0.0000	33.1500	103.8400	21.0	3.4	118	9.93±1.51e+14	0.65±0.08	356.4±144.7
2017-08-08	16:37:0.0000	33.2700	103.7900	11.0	2.4	3	8.75±0.94e+15	0.17±0.01	55.2±13.1
2017-08-08	16:43:0.0000	33.1300	103.8800	8.0	2.0	24	8.39±4.10e+13	0.81±0.16	58.2±45.6
2017-08-08	17:20:0.0000	33.1200	103.8900	11.0	2.7	69	1.63±0.23e+14	0.76±0.10	94.8±38.6
2017-08-08	17:39:0.0000	33.2700	103.8000	9.0	2.7	73	4.66±0.69e+14	0.51±0.05	78.9±26.9
2017-08-08	17:42:0.0000	33.1700	103.8400	22.0	2.3	4	2.18±1.09e+16	0.12±0.02	50.1±39.2
2017-08-08	17:43:0.0000	33.2200	103.8000	2.0	2.7	43	4.30±0.52e+14	0.50±0.07	72.6±29.7

Continued

Epicentral parameters					M_L	Number of recording stations	Inverted source parameters		
Data (a-mo-d)	Time (UTC)	Latitude (°N)	Longitude (°E)	Depth (km)			Seismic moment M_0 (N·m)	Corner frequency f_c (Hz)	Stress drop $\Delta\sigma$ (kPa)
2017-08-08	19:59:0.0000	33.2900	103.8100	18.0	2.8	82	3.87±0.26e+14	0.57±0.06	93.1±27.9
2017-08-08	21:14:0.0000	33.2100	103.8100	11.0	2.7	92	5.07±0.36e+14	0.52±0.05	95.6±28.2
2017-08-08	21:16:0.0000	33.3100	103.7600	14.0	3.2	109	8.28±0.82e+14	0.68±0.05	337.0±79.8
2017-08-08	21:26:0.0000	33.3400	103.7500	3.0	2.1	31	2.48±0.69e+14	0.53±0.06	49.7±22.7
2017-08-08	21:35:0.0000	33.1500	103.8600	19.0	2.0	99	2.56±0.32e+14	0.83±0.11	195.5±79.1
2017-08-08	21:37:0.0000	33.1300	103.8600	23.0	4.3	145	1.54±0.17e+15	0.66±0.06	588.2±165.5
2017-08-08	21:41:0.0000	33.1700	103.8500	16.0	3.2	51	1.76±0.20e+15	0.52±0.07	329.3±132.7
2017-08-08	22:14:0.0000	33.1200	103.8700	10.0	2.6	62	2.09±0.26e+14	0.65±0.08	76.2±28.1
2017-08-08	22:24:0.0000	33.1500	103.8400	18.0	3.0	88	2.96±0.28e+14	0.80±0.09	198.4±73.2
2017-08-08	22:49:0.0000	33.3100	103.7700	4.0	3.2	120	6.87±0.62e+14	0.84±0.12	533.3±227.9
2017-08-08	22:50:0.0000	33.3000	103.7700	4.0	2.2	110	8.46±0.70e+14	0.78±0.07	525.0±148.6
2017-08-08	22:51:0.0000	33.0100	103.9900	15.0	2.2	39	1.34±0.14e+15	0.63±0.08	435.5±172.6
2017-08-08	23:23:0.0000	33.2600	103.8000	1.0	2.0	14	7.89±2.00e+14	0.36±0.04	49.8±20.2
2017-08-09	0:10:0.0000	33.1400	103.8600	17.0	3.8	132	3.04±0.95e+16	0.14±0.03	103.3±68.8
2017-08-09	0:29:0.0000	33.3000	103.7900	18.0	3.9	129	4.34±0.64e+15	0.50±0.07	734.8±330.7
2017-08-09	1:22:0.0000	33.1600	103.8400	21.0	3.6	137	2.61±0.37e+15	0.49±0.06	409.3±162.2
2017-08-09	1:32:0.0000	33.2800	103.7400	16.0	3.7	117	1.49±0.33e+15	0.58±0.10	387.3±208.4
2017-08-09	2:17:0.0000	33.1000	103.8500	5.0	4.9	155	8.68±0.88e+15	0.49±0.06	1331.8±546.7
2017-08-09	3:7:0.0000	33.3400	103.7600	6.0	2.3	56	7.24±0.90e+14	0.41±0.03	64.4±17.2
2017-08-09	4:43:0.0000	33.1500	103.8800	22.0	2.7	62	2.36±0.26e+14	0.59±0.05	64.0±17.8
2017-08-09	6:14:0.0000	33.3200	103.7700	5.0	2.1	38	4.15±1.42e+14	0.45±0.06	51.1±27.9
2017-08-09	9:22:0.0000	33.2400	103.7800	5.0	2.4	40	2.37±0.34e+14	0.59±0.05	63.6±18.8
2017-08-09	10:15:0.0000	33.1200	103.8700	19.0	2.2	37	3.82±0.47e+14	0.48±0.03	54.9±13.5
2017-08-09	10:21:0.0000	33.1500	103.8600	17.0	2.2	12	1.37±0.42e+16	0.15±0.02	66.2±33.0
2017-08-09	11:51:0.0000	33.3200	103.7900	3.0	2.3	16	7.21±3.57e+13	0.83±0.14	53.9±37.9
2017-08-09	12:3:0.0000	33.1600	103.8500	17.0	3.0	75	2.69±0.18e+14	0.86±0.10	223.0±78.2
2017-08-09	12:30:0.0000	33.3300	103.7900	2.0	2.2	10	2.52±0.77e+15	0.25±0.03	52.6±24.4
2017-08-09	16:27:0.0000	33.1900	103.8300	18.0	2.4	57	2.43±0.49e+14	0.56±0.06	54.8±20.1
2017-08-09	17:28:0.0000	33.2100	103.8000	5.0	2.5	43	3.31±0.52e+14	0.50±0.03	53.0±13.8
2017-08-09	17:44:0.0000	33.1500	103.8600	18.0	2.2	36	1.35±0.38e+14	0.65±0.07	49.2±21.6
2017-08-09	18:30:0.0000	33.1600	103.8400	23.0	3.0	90	4.70±0.39e+14	0.52±0.06	86.8±30.0
2017-08-09	19:2:0.0000	33.2500	103.7700	22.0	3.6	131	1.37±0.15e+15	0.62±0.08	427.2±173.7
2017-08-09	19:6:0.0000	33.1500	103.8400	10.0	2.8	23	3.75±0.45e+14	0.61±0.07	109.3±41.9
2017-08-09	19:14:0.0000	33.2500	103.7800	18.0	2.3	46	3.30±0.52e+14	0.49±0.04	51.3±14.1
2017-08-09	21:5:0.0000	33.1400	103.8600	20.0	4.6	147	3.29±0.28e+15	0.56±0.07	772.4±283.7
2017-08-09	21:6:0.0000	33.1500	103.8400	17.0	2.9	153	5.70±0.68e+15	0.47±0.06	755.9±316.3
2017-08-09	22:57:0.0000	33.3200	103.7600	4.0	2.1	8	1.49±0.50e+14	0.64±0.09	51.9±28.4

Continued

Epicentral parameters					M_L	Number of recording stations	Inverted source parameters		
Data (a-mo-d)	Time (UTC)	Latitude (°N)	Longitude (°E)	Depth (km)			Seismic moment M_0 (N·m)	Corner frequency f_c (Hz)	Stress drop $\Delta\sigma$ (kPa)
2017-08-09	23:42:0.0000	33.1900	103.8400	10.0	2.0	30	2.28±1.66e+14	0.57±0.12	54.3±52.5
2017-08-10	1:6:0.0000	33.2500	103.7800	11.0	2.2	34	5.10±1.39e+14	0.41±0.04	47.7±19.1
2017-08-10	1:40:0.0000	33.2300	103.7500	5.0	2.3	44	4.46±0.59e+14	0.55±0.05	94.9±27.3
2017-08-10	1:52:0.0000	33.2700	103.7900	15.0	2.3	49	2.77±0.38e+14	0.72±0.06	135.9±40.1
2017-08-10	1:54:0.0000	33.1800	103.8400	14.0	3.4	108	6.23±0.57e+14	0.93±0.12	659.0±268.5
2017-08-10	5:29:0.0000	33.1700	103.8300	13.0	2.1	37	3.77±1.05e+14	0.47±0.05	50.6±20.7
2017-08-10	6:18:0.0000	33.1600	103.8400	22.0	2.1	20	1.31±0.42e+15	0.31±0.04	51.7±25.8
2017-08-10	7:30:0.0000	33.1500	103.8500	12.0	2.9	76	6.32±0.65e+14	0.52±0.07	116.9±47.4
2017-08-10	7:46:0.0000	33.0900	103.8900	12.0	2.6	51	1.09±0.17e+15	0.37±0.03	70.4±22.2
2017-08-10	9:38:0.0000	33.2900	103.7500	11.0	3.0	78	4.94±0.44e+14	0.68±0.07	207.6±66.1
2017-08-10	9:48:0.0000	33.2200	103.8800	20.0	4.3	145	1.76±0.18e+15	0.77±0.10	1069.7±418.5
2017-08-10	10:27:0.0000	33.1500	103.8500	14.0	2.5	41	1.42±0.16e+14	0.85±0.08	113.7±34.0
2017-08-10	13:12:0.0000	33.1500	103.8500	9.0	2.4	39	2.97±0.44e+14	0.54±0.05	62.8±19.1
2017-08-11	0:5:0.0000	33.1800	103.8400	17.0	2.9	73	3.39±0.39e+14	0.79±0.09	219.4±77.8
2017-08-11	2:37:0.0000	33.1300	103.8700	18.0	2.2	30	3.26±0.76e+14	0.50±0.05	53.5±21.5
2017-08-11	7:5:0.0000	33.3000	103.7700	12.0	2.1	11	2.75±1.10e+14	0.55±0.08	59.4±36.0
2017-08-11	11:26:0.0000	33.1200	103.8600	16.0	3.5	109	5.88±0.40e+14	0.90±0.11	567.3±205.9
2017-08-11	11:59:0.0000	33.1300	103.8800	17.0	2.7	59	1.67±0.36e+15	0.29±0.03	53.8±18.3
2017-08-11	13:36:0.0000	33.3200	103.7400	16.0	2.5	40	5.60±1.61e+14	0.41±0.04	50.8±22.1
2017-08-11	13:42:0.0000	33.2500	103.7900	14.0	2.1	16	2.32±0.88e+15	0.26±0.03	54.1±28.7
2017-08-11	14:0:0.0000	33.2200	103.8200	12.0	2.2	26	1.42±0.40e+14	0.64±0.08	48.8±22.1
2017-08-11	23:56:0.0000	33.1100	103.8600	16.0	3.7	122	7.57±0.51e+14	0.85±0.08	601.3±178.0
2017-08-12	1:46:0.0000	33.1500	103.8500	15.0	2.1	22	1.11±0.29e+14	0.71±0.08	51.7±22.0
2017-08-12	3:42:0.0000	33.1600	103.8400	13.0	2.2	47	3.41±0.50e+14	0.50±0.04	55.1±17.0
2017-08-12	9:46:0.0000	33.1200	103.8600	15.0	2.7	61	2.53±0.27e+14	0.65±0.07	91.5±31.8
2017-08-12	19:57:0.0000	33.1600	103.8500	12.0	2.5	46	2.70±0.83e+14	0.52±0.06	51.4±24.8
2017-08-13	5:24:0.0000	33.1600	103.8500	11.0	2.1	15	1.55±0.39e+14	0.64±0.08	53.4±23.0
2017-08-13	14:38:0.0000	33.0900	103.8900	16.0	3.4	111	5.66±0.47e+14	0.83±0.09	426.1±140.9
2017-08-13	20:13:0.0000	33.2000	103.8300	10.0	2.7	70	2.40±0.27e+14	0.66±0.06	90.1±28.1
2017-08-13	21:18:0.0000	33.1700	103.8300	12.0	2.2	49	1.55±0.29e+14	0.64±0.05	53.4±16.5
2017-08-14	8:16:0.0000	33.2000	103.8200	14.0	2.6	47	3.97±0.44e+14	0.48±0.03	56.4±12.6
2017-08-14	10:39:0.0000	33.1000	103.9000	20.0	2.1	28	5.60±1.11e+14	0.42±0.03	54.6±17.2
2017-08-14	14:30:0.0000	33.2600	103.7900	13.0	2.3	46	4.21±0.61e+14	0.46±0.04	54.5±15.6
2017-08-15	8:6:0.0000	33.1200	103.8700	18.0	2.8	66	5.55±1.05e+14	0.49±0.05	88.3±31.3
2017-08-15	16:51:0.0000	33.1400	103.8400	10.0	2.6	67	2.47±0.24e+14	0.64±0.05	85.6±22.4
2017-08-15	18:2:0.0000	33.1100	103.8700	6.0	2.1	46	1.49±0.35e+14	0.63±0.06	48.9±17.7
2017-08-15	21:26:0.0000	33.1700	103.8500	11.0	2.1	34	1.72±0.46e+14	0.60±0.06	48.9±18.7

Continued

Epicentral parameters					M_L	Number of recording stations	Inverted source parameters		
Data (a-mo-d)	Time (UTC)	Latitude (°N)	Longitude (°E)	Depth (km)			Seismic moment M_0 (N·m)	Corner frequency f_c (Hz)	Stress drop $\Delta\sigma$ (kPa)
2017-08-16	6:59:0.0000	33.1800	103.8200	10.0	2.3	36	2.90±0.58e+14	0.55±0.07	63.4±25.9
2017-08-16	9:39:0.0000	33.1600	103.8400	15.0	2.6	44	6.80±1.15e+14	0.39±0.03	52.7±15.8
2017-08-16	19:6:0.0000	33.1400	103.8500	15.0	2.3	28	1.07±0.51e+15	0.33±0.06	49.2±35.4
2017-08-16	23:49:0.0000	33.2400	103.8000	11.0	2.0	3	7.60±1.52e+15	0.19±0.02	72.7±28.9
2017-08-17	5:54:0.0000	33.3000	103.7600	13.0	2.1	10	2.28±1.30e+14	0.56±0.10	52.5±41.4
2017-08-18	10:58:0.0000	33.3400	103.7300	10.0	2.0	23	2.40±0.66e+14	0.55±0.06	52.3±23.1
2017-08-18	19:58:0.0000	33.1000	103.8900	16.0	2.1	43	1.66±0.36e+14	0.61±0.06	50.2±18.0
2017-08-19	11:52:0.0000	33.1200	103.9000	12.0	3.3	123	8.31±0.89e+14	0.74±0.08	443.7±148.9
2017-08-21	2:11:0.0000	33.1700	103.8200	12.0	2.2	38	5.10±0.91e+14	0.45±0.05	61.6±23.0
2017-08-21	4:16:0.0000	33.1800	103.8400	11.0	2.2	28	5.82±1.85e+14	0.40±0.04	48.6±22.4
2017-08-22	4:0:0.0000	33.2200	103.8100	9.0	2.2	36	5.98±0.97e+14	0.42±0.04	57.8±18.9
2017-08-22	20:45:0.0000	33.3200	103.7800	14.0	2.7	58	5.61±1.37e+14	0.43±0.05	59.8±25.8
2017-08-24	0:34:0.0000	33.2700	103.7700	5.0	2.1	21	8.23±2.47e+14	0.37±0.05	55.7±27.3
2017-08-24	18:32:0.0000	33.2100	103.8200	16.0	2.1	13	2.59±0.97e+15	0.25±0.03	55.0±29.9
2017-08-24	20:28:0.0000	33.0800	103.9000	10.0	3.0	92	5.31±0.52e+14	0.48±0.04	78.6±21.2
2017-08-24	20:39:0.0000	33.0700	103.9100	14.0	2.1	40	4.82±1.81e+14	0.43±0.07	51.6±32.7
2017-08-25	6:23:0.0000	33.2800	103.7800	11.0	2.1	6	1.09±0.39e+15	0.33±0.04	52.7±25.5
2017-08-25	22:31:0.0000	33.0800	103.9000	13.0	2.4	51	1.94±0.39e+14	0.61±0.06	58.7±21.7
2017-08-27	0:58:0.0000	33.2200	103.7500	15.0	3.3	112	1.35±0.11e+15	0.54±0.06	285.9±93.9
2017-08-27	10:3:0.0000	33.5400	104.8600	15.0	2.4	42	2.02±0.29e+14	0.61±0.05	60.3±16.2
2017-08-27	19:2:0.0000	33.3000	103.8000	11.0	2.9	90	5.19±0.93e+14	0.56±0.08	119.9±52.9
2017-08-31	5:50:0.0000	32.7300	104.1100	13.0	2.4	43	3.45±0.69e+14	0.48±0.04	49.5±15.7
2017-09-02	16:41:0.0000	33.2000	103.8200	14.0	2.0	24	1.95±0.74e+14	0.58±0.08	51.2±29.3
2017-09-05	17:57:0.0000	33.2500	103.7800	16.0	3.2	124	8.25±0.66e+14	0.60±0.04	236.4±55.1
2017-09-06	2:4:0.0000	33.0800	103.9000	15.0	2.7	76	4.00±0.39e+14	0.54±0.05	82.3±24.6
2017-09-06	12:20:0.0000	33.1600	103.8500	14.0	2.1	28	1.69±0.38e+14	0.62±0.07	53.8±21.1
2017-09-07	4:15:0.0000	33.1100	103.8900	12.0	3.3	108	5.01±0.40e+14	0.80±0.07	343.3±92.3
2017-09-07	17:54:0.0000	33.0900	103.9000	19.0	2.2	31	1.01±1.08e+15	0.34±0.09	52.7±70.4
2017-09-09	7:24:0.0000	33.2700	103.7900	10.0	2.1	27	1.10±0.35e+15	0.33±0.04	50.5±24.0
2017-09-09	15:58:0.0000	33.3100	103.7500	15.0	2.7	64	2.90±0.93e+14	0.53±0.08	56.5±31.2
2017-09-10	9:22:0.0000	33.1600	103.8500	13.0	2.1	9	6.47±2.62e+14	0.39±0.06	51.5±31.4
2017-09-12	0:35:0.0000	33.2000	103.8300	13.0	2.1	22	2.34±1.52e+16	0.12±0.03	55.1±52.0
2017-09-12	19:31:0.0000	33.2000	103.8100	13.0	2.7	57	5.31±0.95e+14	0.43±0.03	53.8±15.4
2017-09-12	23:59:0.0000	33.2700	103.7700	7.0	3.1	85	8.41±0.87e+14	0.46±0.04	105.0±30.9
2017-09-18	15:37:0.0000	33.2400	103.7600	9.0	2.8	68	8.10±3.05e+14	0.40±0.07	68.5±45.4
2017-09-26	21:43:0.0000	33.1200	103.8800	11.0	2.0	17	8.84±3.56e+13	0.76±0.13	51.6±33.1
2017-09-26	21:53:0.0000	33.1200	103.8800	10.0	2.2	28	1.23±0.48e+14	0.68±0.08	50.9±26.7

Continued

Epicentral parameters					M_L	Number of recording stations	Inverted source parameters		
Data (a-mo-d)	Time (UTC)	Latitude (°N)	Longitude (°E)	Depth (km)			Seismic moment M_0 (N·m)	Corner frequency f_c (Hz)	Stress drop $\Delta\sigma$ (kPa)
2017-10-02	10:53:0.0000	33.0800	103.9100	19.0	2.2	13	1.81±0.36e+14	0.61±0.06	54.6±20.2
2017-10-04	19:18:0.0000	33.3200	103.7800	9.0	3.2	108	6.39±0.58e+14	0.63±0.05	207.8±56.8
2017-10-06	2:19:0.0000	33.2800	103.8000	15.0	2.1	14	6.28±1.85e+14	0.40±0.05	51.0±24.1
2017-10-06	10:25:0.0000	33.2300	103.8000	20.0	4.1	133	1.03±0.10e+15	0.86±0.07	859.8±223.3
2017-10-08	8:4:0.0000	33.3300	103.7700	7.0	2.1	9	1.03±0.44e+14	0.74±0.11	54.9±34.7
2017-10-08	21:35:0.0000	33.1300	103.8500	13.0	2.1	28	1.52±1.44e+15	0.30±0.05	52.0±56.4
2017-10-14	3:2:0.0000	33.2400	103.7800	7.0	3.1	67	1.29±0.16e+15	0.37±0.04	88.6±33.7
2017-10-19	4:37:0.0000	33.1300	103.8600	13.0	2.2	26	6.36±1.29e+14	0.39±0.03	51.1±16.9
2017-10-31	14:39:0.0000	33.1200	103.8800	9.0	2.2	44	5.57±1.46e+14	0.41±0.05	52.3±22.3
2017-11-02	12:37:0.0000	33.3200	103.7800	11.0	2.1	35	1.18±0.31e+14	0.69±0.07	50.6±21.1
2017-11-06	21:31:0.0000	33.1700	103.8000	10.0	4.9	154	1.02±0.12e+16	0.41±0.04	910.9±286.4
2017-11-07	6:43:0.0000	33.2400	103.7900	14.0	2.2	27	3.66±1.43e+14	0.48±0.07	53.3±32.2
2017-11-17	5:44:0.0000	33.2400	103.7800	10.0	2.8	57	3.39±0.44e+14	0.55±0.06	74.9±24.6
2017-11-21	14:9:0.0000	32.9900	103.9800	13.0	2.5	48	1.39±0.13e+14	0.75±0.07	77.0±22.9
2017-11-29	12:52:0.0000	33.1500	103.8600	18.0	2.9	78	2.20±0.20e+14	0.94±0.12	239.4±92.7
2017-12-03	18:31:0.0000	33.1800	103.8200	11.0	2.2	62	5.15±0.88e+14	0.43±0.03	52.4±14.4
2017-12-10	0:14:0.0000	33.2800	103.7400	15.0	2.7	56	3.30±0.37e+14	0.53±0.04	63.4±17.2
2018-01-03	16:19:0.0000	33.3100	103.7700	14.0	2.6	59	3.38±0.68e+14	0.50±0.05	56.8±19.8
2018-01-17	23:58:0.0000	33.3200	103.8300	8.0	2.2	47	1.60±0.71e+15	0.28±0.04	47.1±28.2
2018-01-26	2:14:0.0000	33.2400	103.7700	10.0	2.7	61	1.18±0.16e+15	0.33±0.02	53.4±14.0

for stress drops of moderate to large intraplate earthquakes (Allmann and Shearer, 2009) but was notably larger than the 3.8 MPa value estimated for the mainshock based on strong motion observations (Wang et al., 2017a). The difference may be due to several reasons, including (1) the Lg-wave and strong motion data cover different frequency bands; (2) the estimated stress drop is sensitive to uncertainties in the M_0 and f_c measurements; (3) the theoretical source model may be oversimplified (Gallovič and Valentová, 2020). In this study, the source parameters, e.g., the seismic moment, corner frequency and stress drop, were measured for the entire sequence using the same method, which allows us to investigate the relative variations in these parameters among the mainshock and its aftershocks and to explore their spatial and temporal variations during the development of the sequence.

4 Discussion

The stress drops diminished as the seismicity decreased in intensity, and the temporal variation highlights the overall decay of the stress drop, especially the abrupt decrease since the mainshock (Figure 4). This pattern possibly indicates that the accumulated energy was relatively fully released by the mainshock (Wang et al., 2018). The map of stress drop reveals very large variations occurring over short length scales, which may indicate complicated source mechanisms for the 2017 Jiuzhaigou earthquake and its aftershocks (Figure 5). Close to the mainshock, which had the highest stress drop of 7.1 MPa, the aftershocks were relatively sparser, and their stress drops were less than the median value. Furthermore, the less-than-median stress drops seemingly concentrated near the trace of the major seismogenic fault, which could be inferred from the major axis of the aftershock zone, while higher stress drops appeared off the trace of this fault. The coseismic displacements inverted from geodetic data suggested that the slip on the seismogenic fault was primarily concentrated at approximately 7–15 km depth (Ji et al., 2017; Wang et al., 2017b; Wang et al., 2018). On the

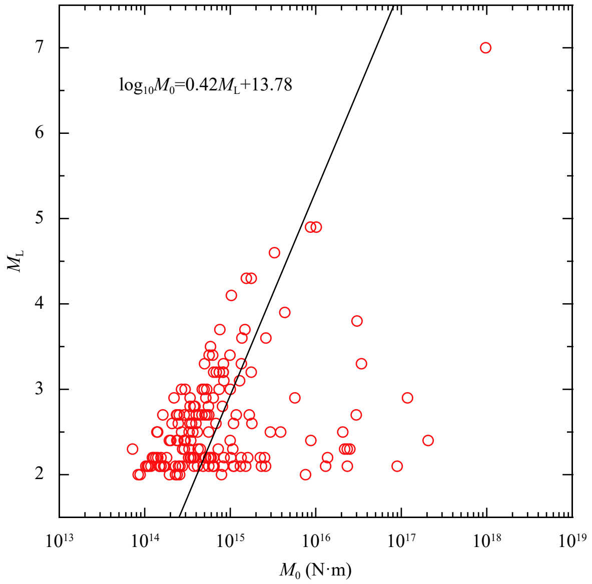

Figure 3 Plot of magnitude M_L versus seismic moment M_0. Circles denote event measurements and the black line represents the relationship between M_L and M_0 obtained using linear regression

fault plane with a dip angle of 70° obtained from focal mechanism solution (Wang et al., 2017b), onto which all events were projected, there appeared to be no clear or strong correlation between the stress drop and depth, but we observed a tendency that aftershocks with stress drops higher than the median value of 59 kPa were more likely to occur at depths of ~15 km (corresponding to a distance of ~13 km along dip), just below the depth of significant slip (Figure 6). These observations could be related to the fact that the energy accumulated within the seismogenic fault associated with the Jiuzhaigou earthquake was relatively thoroughly released by coseismic displacement, and thus, the aftershocks off the seismogenic fault and outside of the zone of large slip released larger amounts of stress than those on the fault and within the zone of large slip.

The assumption of earthquake scaling self-similarity, suggesting that the physics of earthquakes is independent of their sizes, implies that the stress drop remains constant over earthquakes with a wide range of magnitudes (Aki, 1967). It can be predicted that on a log-log plot, the shape of all source spectra will be identical with offset along a f^{-3} line (Allmann and Shearer, 2009; Prieto et al., 2004; Shearer, 2009). The self-similarity appears to be roughly true for most earthquakes except for very large ones. Shearer et al. (2006) found little dependence of stress drop on moment and suggested that over 60,000 earthquakes in southern California with M_L magnitudes ranging from 1.5 to 3.1 were self-similar. Allmann and Shearer (2007) found that the stress drops of over 40,000 earthquakes remained nearly constant with moment, implying self-similarity across earthquakes with M_L magnitudes between 0.5 and 3.0 in central California. At the global scale, self-similarity in moderate to large earthquakes has also been suggested (Allmann and Shearer, 2009). However, a strong dependence of stress drop on earthquake size was observed at small scales, which could be related to the local stress regime (Oth, 2013). Moreover, Zhao et al. (2011) observed

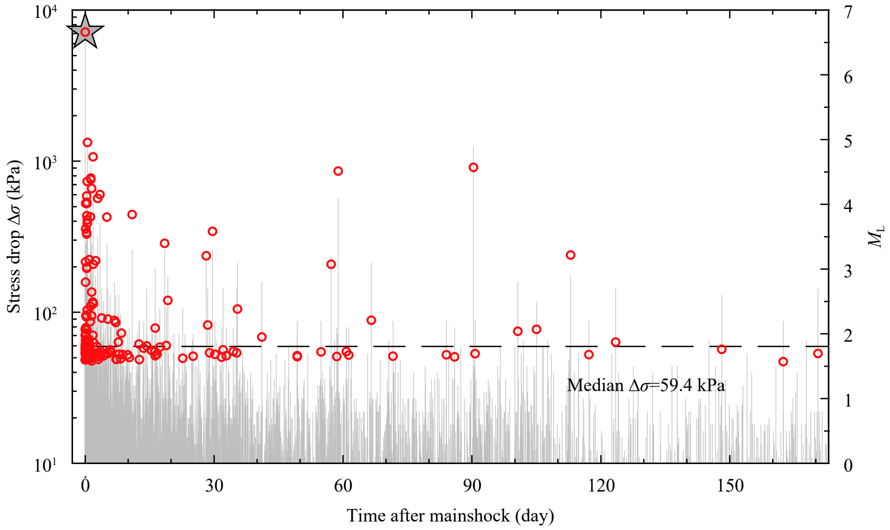

Figure 4 Temporal variation in the stress drops for the 2017 Jiuzhaigou earthquake and its aftershocks. The gray star denotes the mainshock, and the red circles represent the computed stress drops for aftershocks. The median stress drop is marked by the horizontal dashed line. For comparison, the seismicity is shown by vertical gray lines, each representing an earthquake with the height corresponding to the magnitude. The stress drop values decayed as the seismic activity gradually diminished

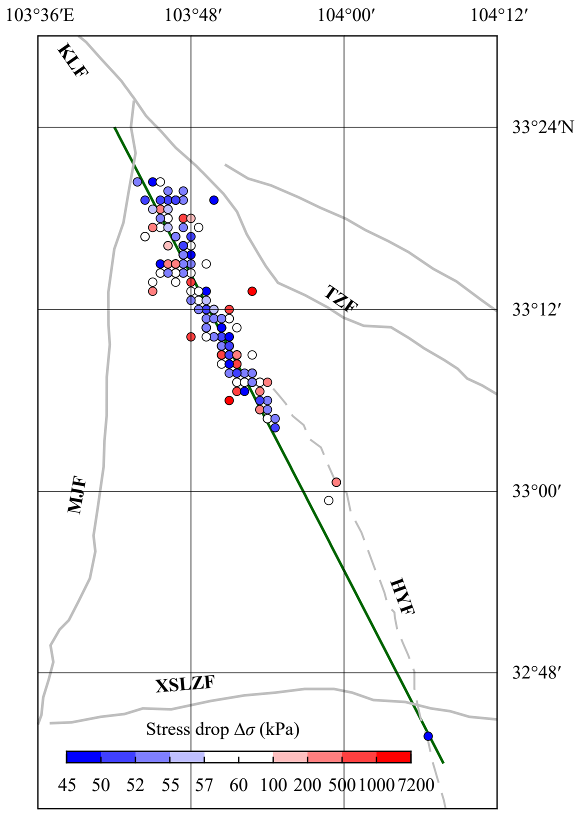

Figure 5 Map of the distribution of stress drops. Circles denote the stress drops of aftershocks. Events that are very close to the epicenter of the mainshock and near the major axis of the aftershock zone generally exhibit lower-than-median stress drops, while events off the seismogenic fault are more likely to have higher stress drops. The green line denotes the profile onto which all events are projected. The abbreviations are as follows: KLF is Kunlun fault; TZF is Tazang fault; HYF is Huya fault; MJF is Minjiang fault; XSLZF is Xueshanliangzi fault

that the stress drop increases with earthquake magnitude, favoring a nonconstant stress drop model and thus rejecting the assumption of self-similarity. In this study, a constant stress drop can be calculated from linear regression between $\log_{10}f_c$ and $\log_{10}M_0$ with a fixed slope of –3, and we found that the constant average stress drop for the 2017 Jiuzhaigou earthquake sequence was 93.0 kPa (Figure 7). However, by careful investigation, these events can be further grouped into two clusters in Figure 7, with blue symbols representing events with stress drops lower than the regional average of 93.0 kPa and red symbols representing events with stress drops higher than the regional average (Figure 7). Performing linear regression on each of the clusters of events, we obtained values of 57.4 kPa and 318.9 kPa, which provided a better fit for both clusters of events. For the blue cluster, the values of stress drop remained nearly constant versus the seismic moment over 3 orders of magnitude, indicating that these aftershocks were self-similar in their source physics. These events could be related to the left-lateral slip motion driven by the eastward expansion of the Tibetan Plateau (Sun et al., 2018). For the red cluster, the values of stress drop were systematically higher and more scattered, especially for the mainshock, which had a significantly high stress drop. This may be related to the very large magnitudes that caused the rupture behaviors of these events to differ from those of other moderate events in terms of the aspect ratios. The two groups of events were characterized by different levels of self-similarity, which can be attributed to a nonconstant stress drop (Taylor et al., 2002). The level can be quantified by the deviation of slope from –3 when performing linear regression between $\log_{10}f_c$ and $\log_{10}M_0$ (Kanamori and Rivera, 2004). Overall fitting produced a slope of –2.52, but separate linear regression provided better fit for both clusters of events (Figure 8). For the red cluster, the slope was less than –3, demonstrating that the stress drop values increased with earthquake size. In contrast, the slope for the blue cluster was –2.97, which are very close to –3, suggesting that the stress drop of events in this cluster was nearly constant and that these events were self-similar. The electrical structure obtained using magnetotelluric imaging suggested that anomalies of high conductivity extend across the northern part of the Huya fault, with its top boundary at depths of ~10–20 km in the Jiuzhaigou earthquake source region (Sun et al., 2017; Zhao et al., 2012). The majority of events in the blue cluster (i.e., 86 of 120 events) were located deeper than 10 km and were very likely to be affected by the high-conductivity structure. This improves our understanding of the observed low stress drop values of events in the blue cluster because the presence of elevated fluid content, as indicated by the high-conductivity anomaly, could reduce the stress applied on the faults by increasing the fluid pore pressure (e.g., Sumy et al., 2017). However, because the epicentral depths of the Jiuzhaigou earthquake sequence were obtained from a catalog and because the depth resolution of the magnetotelluric imaging might be limited, detailed investigations into the impact of the presumed viscous crustal flow on the seismogenic dynamics of local seismicity are still required. These investigations should include analysis based on high-precision relocation results and further studies on the fine-scale local electrical structure as constrained by high-resolution magnetotelluric images.

5 Conclusions

The stress drop is one of the fundamental parameters

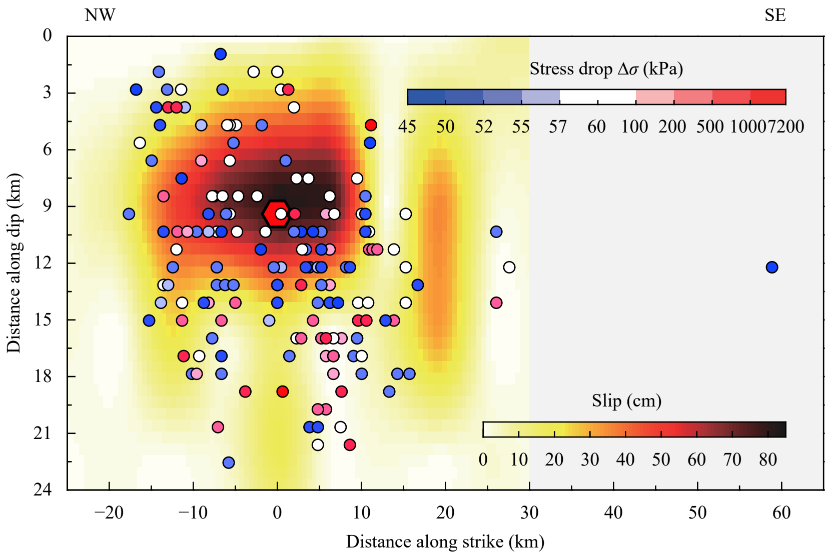

Figure 6 Spatial variation in stress drop and slip distribution (Wang et al., 2017b) on the seismogenic fault plane. Each circle represents an earthquake and is filled according to its stress drop value. Higher-than-median stress drops more likely appear for aftershocks at depths deeper than ~15 km (corresponding to ~13 km along dip) and in areas where coseismic slip was less than ~ 40 cm. The red hexagon denotes the mainshock, and the light gray area on the right represents a lack of coseismic slip data coverage

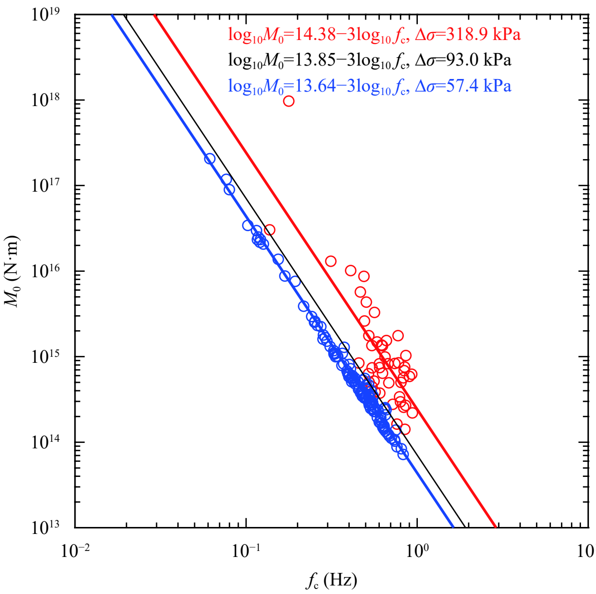

Figure 7 Seismic moment M_0 versus corner frequency f_c. Assuming the scaling relationship of $M_0 \propto f^{-3}$ and a constant stress drop model, linear regression yields an average stress drop for the region near the Jiuzhaigou earthquake of 93 kPa (black line). These events can be divided into two clusters according to the average stress drop (blue circles denote events with stress drops lower than the average, and red circles denote events with stress drops higher than the average). Separate linear fitting for each cluster yields a stress drop of 57.4 kPa for the events in the blue cluster (blue line) and a stress drop of 318.9 kPa for the events in the red cluster (red line)

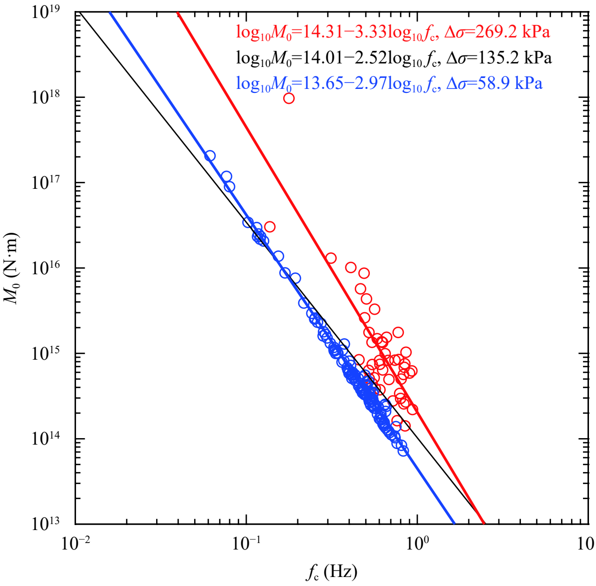

Figure 8 Seismic moment M_0 versus corner frequency f_c. The grouped red and blue clusters of earthquakes are same as those in Figure 7. The results of linear regression between $\log_{10}f_c$ and $\log_{10}M_0$ for all events, blue cluster and red cluster are denoted by black, blue and red lines, respectively. Linear regression suggests that the events in the blue cluster, with a scaling factor very close to –3 and a nearly constant stress drop, exhibit self-similarity. The events in the red cluster are characterized by a scaling factor less than –3, which means that the stress drop increases with increasing seismic moment instead of exhibiting self-similarity, a possible indicator of different source physics

characterizing the dynamic rupture of an earthquake. It is also useful in investigating the process of stress field adjustment after a major earthquake through the analysis of its aftershock sequence. The stress drop of a seismic event can be estimated from seismic observations through the seismic moment and corner frequency of the source spectrum. However, effects from the attenuation along the propagation path can distort the shape of the source spectrum, especially at higher frequencies and in regions with strong lateral attenuation variations. In this study, we used a high-resolution broadband Lg-wave Q model to compensate for the effect of attenuation in Lg-wave source spectra. The corrected data were fitted with the theoretical source model to obtain source parameters for the 2017 Jiuzhaigou earthquake and its 166 aftershocks with magnitude M_{L} greater than 2.0. The seismic moment and corner frequency were then determined using the bootstrap method, and the stress drop was estimated for individual events. The obtained seismic moments were linearly related to the magnitude M_{L}. The Brune-type stress drop was calculated for individual events. The stress drop for the mainshock was 7.1 MPa, while the median value of stress drops from all aftershocks was less than 60 kPa. The temporal variation in the stress drop demonstrated an abrupt decay after the mainshock. The aftershocks very close to the mainshock, near the major axis of the aftershock zone, or within the zone with large coseismic slip exhibited relatively low stress drops. The above observations suggested that the stress energy accumulated by the major seismogenic fault was largely released by the mainshock. Based on the relationship of the seismic moment versus the corner frequency on the log-log scale, the aftershocks can be separated into two groups, one of which was characterized by self-similarity with a nearly constant stress drop of approximately 58 kPa and a scaling relation of $M_0 \propto f^{-2.97}$. The events in the second cluster exhibited increasing stress drop with increasing seismic moment, possibly suggestive of different source physics related to dissipation of the energy on the major seismogenic fault and localized stress heterogeneities resulting from complicated tectonic activities.

Acknowledgments

The authors are grateful to the two anonymous reviewers, whose constructive comments have improved this paper. This work was supported by the Special Fund of China Seismic Experimental Site (Nos. 2019CSES0103, 2018CESE0102 and 2016CESE0203), the National Natural Science Foundation of China (Nos. 41630210, 41674060 and 41974054), and the 13th Five-year Informatization Plan of Chinese Academy of Sciences (grant No. XXH13505-06). Waveforms used in this study were collected from the Data Management Centre of China, National Seismic Network at Institute of Geophysics, China Earthquake Administration (SEISDMC, doi:10.7914/SN/CB) (Zheng et al., 2010) and the Incorporated Research Institutions for Seismology Data Management Center (http://www.iris.edu, accessed August 2019). The focal mechanisms were retrieved from the global Centroid-Moment-Tensor (CMT) catalog (http://www.globalcmt.org, accessed August 2019) (Dziewonski et al., 1981; Ekstrom et al., 2012). Some figures were made using Generic Mapping Tools (https://forum.generic-mapping-tools.org/, accessed March 2020) (Wessel et al., 2013).

References

Abercrombie RE and Rice JR (2005) Can observations of earthquake scaling constrain slip weakening? Geophys J Int **162**: 406–424

Aki K (1967) Scaling law of seismic spectrum. J Geophys Res **72**: 1217–1 231

Allmann BP and Shearer PM (2007) Spatial and temporal stress drop variations in small earthquakes near Parkfield, California. J Geophys Res **112**: B04305

Allmann BP and Shearer PM (2009) Global variations of stress drop for moderate to large earthquakes. J Geophys Res **114**: B01310

Bao X, Song X and Li J (2015) High-resolution lithospheric structure beneath Mainland China from ambient noise and earthquake surface-wave tomography. Earth Planet Sci Lett **417**: 132–141

Brune JN (1970) Tectonic stress and the spectra of seismic shear waves from earthquakes. J Geophys Res **75**: 4 997–5 009

Chen W, Qiao XJ and Liu G (2018) Study on the coseismic slip model and Coulomb stress of the 2017 Jiuzhaigou M_{S}7.0 earthquake constrained by GNSS and InSAR measurements. Chin J Geophys **61**(5): 2 122–2132 (in Chinese with English abstract)

Dziewonski AM, Chou TA and Woodhouse JH (1981) Determination of earthquake source parameters from waveform data for studies of global and regional seismicity. J Geophys Res **86**: 2 825–2 852

Efron B (1983) Estimating the error rate of a prediction rule: Improvement on cross-validation. J Am Stat Assoc **78**: 316–331

Ekstrom G, Nettles M and Dziewonski AM (2012) The global CMT project 2004–2010: Centroid-moment tensors for 13,017 earthquakes. Phys Earth Planet Inter **200**: 1–9

Eshelby JD and Peierls RE (1957) The determination of the elastic field of an ellipsoidal inclusion and related problems. Proceedings of the Royal Society of London. Series A. Mathematical, Physical and Engineering Sciences **241**: 376–396

Fang LH, Wu JP, Su JR, Wang MM, Jiang C, Fan LP, Wang WL, Wang CZ and Tan XL (2018) Relocation of mainshock and aftershock sequence of the M_{S}7.0 Sichuan Jiuzhaigou earthquake. Chin Sci Bull **63**: 649–662 (in Chinese with English abstract)

Gallovič F and Valentová L' (2020) Earthquake stress drops from dynamic rupture simulations constrained by observed ground motions. Geophys Res Lett **47**: e2019GL085880

Han L, Cheng J, An Y, Fang L, Jiang C, Chen B, Wu Z, Liu J, Xu X, Liu R, Yao Z, Wang C and Wang Y (2018) Preliminary report on the 8 August 2017 M_S7.0 Jiuzhaigou, Sichuan, China, earthquake. Seismol Res Lett **89**: 557–569

Herrmann RB and Kijko A (1983) Modeling some empirical vertical component Lg relations. Bull Seismol Soc Amer **73**: 151–171

Ji LY, Liu CJ, Xu J, Liu L, Long F and Zhang ZW (2017) InSAR observation and inversion of the seismogenic fault for the 2017 Jiuzhaigou M_S7.0 earthquake in China. Chin J Geophys **60**(10): 4069–4082 (in Chinese with English abstract)

Kanamori H and Rivera L (2004) Static and dynamic scaling relations for earthquakes and their implications for rupture speed and stress drop. Bull Seismol Soc Amer **94**: 314–319

Kirby E, Harkins N, Wang E, Shi X, Fan C and Burbank D (2007) Slip rate gradients along the eastern Kunlun fault. Tectonics **26**: TC2010

Liang J, Sun L and Liu J (2018a) A high precision relocation study of the M_S7.0 Jiuzhaigou earthquake and the aftershocks occurred in 2017. Chin J Geophys **61**: 2152–2162 (in Chinese with English abstract)

Liang SS, Lei JS, Xu ZG, Xu XW and Chen HF (2018b) Relocation of aftershocks of the 2017 Jiuzhaigou, Sichuan, M_S7.0 earthquake and inversion for focal mechanism of the mainshock. Chin J Geophys **61**: 2163–2175 (in Chinese with English abstract)

Liu Z, Tian X, Gao R, Wang G, Wu Z, Zhou B, Tan P, Nie S, Yu G, Zhu G and Xu X (2017) New images of the crustal structure beneath eastern Tibet from a high-density seismic array. Earth Planet Sci Lett **480**: 33–41

Madariaga R (1976) Dynamics of an expanding circular fault. Bull Seismol Soc Amer **66**: 639–666

Oth A (2013) On the characteristics of earthquake stress release variations in Japan. Earth Planet Sci Lett **377**: 132–141

Oth A, Bindi D, Parolai S and Di Giacomo D (2011) Spectral analysis of K-NET and KiK-net data in Japan, Part II: On attenuation characteristics, source spectra and site response of borehole and surface stations. Bull Seismol Soc Amer **101**(2): 667

Paige CC and Saunders MA (1982) LSQR: An algorithm for sparse linear equations and sparse least squares. ACM Trans Math Softw **8**: 43–71

Prieto GA, Shearer PM, Vernon FL and Kilb D (2004) Earthquake source scaling and self-similarity estimation from stacking P and S spectra. J Geophys Res **109**: B08010

Shan XJ, Qu CY, Gong WY, Zhao DZ, Zhang YF, Zhang GH, Song XG, Liu YH and Zhang GF (2017) Coseismic deformation field of the Jiuzhaigou M_S7.0 earthquake from Sentinel-1A InSAR data and fault slip inversion. Chin J Geophys **60**(12): 4527–4536 (in Chinese with English abstract)

Shearer PM (2009) Introduction to seismology, 2nd edn. Cambridge University Press, Cambridge, New York, pp.396

Shearer PM, Prieto GA and Hauksson E (2006) Comprehensive analysis of earthquake source spectra in southern California. J Geophys Res **111**: B06303

Street RL, Herrmann RB and Nuttli OW (1975) Spectral characteristics of the Lg wave generated by central United States earthquakes. Geophys J Int **41**: 51–63

Sumy DF, Neighbors CJ, Cochran ES and Keranen KM (2017) Low stress drops observed for aftershocks of the 2011 M_W5.7 Prague, Oklahoma, earthquake. J Geophys Res **122**: 3813–3834

Sun JB, Yue H, Shen ZK, Fang LH, Zhan Y and Sun XY (2018) 2017 Jiuzhaigou earthquake: a complicated event occurred in a young fault system. Geophys Res Lett **45**: 2230–2240

Sun XY, Zhan Y, Chen XB, Zhao GZ, Zhao LQ, Cui TF and Liu ZY (2017) Seismogenic context of the Jiuzhaigou M_S7.0 earthquake in Sichuan Province inferred from three-dimensional magnetotelluric imaging. The 13th China international geo-electromagnetic workshop, Wuhan, China

Taylor SR, Velasco AA, Hartse HE, Phillips WS, Walter WR and Rodgers AJ (2002) Amplitude corrections for regional sismic discriminants. Pure Appl Geophys **159**: 623–650

Wang HW, Ren YF and Wen RZ (2017a) Source spectra of the 8 August 2017 Jiuzhaigou M_S7.0 earthquake and the quality factor of the epicenter area. Chin J Geophys **60**(10): 4117–4123 (in Chinese with English abstract)

Wang WM, He JK, Hao JL and Yao ZX (2017b) Preliminary result for rupture process of Aug.8, 2017, M7.0 earthquake, Jiuzhaigou, Sichuan, China. http://www.itpcas.ac.cn/xwzx/zhxw/201708/t20170809_4840737.html

Wang YB, Gan WJ and Chen WT (2018) Coseismic displacements of the 2017 Jiuzhaigou M7.0 earthquake observed by GNSS: Preliminary results. Chin J Geophys **61**(1): 161–170 (in Chinese with English abstract)

Wessel P, Smith WHF, Scharroo R, Luis J and Wobbe F (2013) Generic mapping tools: Improved version released. Eos Trans AGU **94**: 409–420

Xu XW, Wu XY, Yu GH, Tan XB and Li K (2017a) Seismo-geological signatures for identifying $M\geq$7.0 earthquake risk areas and their premilimary application in mainland China. Seismology and Geology **39**: 219–275

Xu XW, Chen GH, Wang QX, Chen LC, Ren ZK, Xu C, Wei ZY, Lu RQ, Tan XB and Dong SP (2017b) Discussion on seismogenic structure of Jiuzhaigou earthquake and its implication for current strain state in the southeastern Qinghai-Tibet Plateau. Chin J Geophys **60**(10): 4018–4026 (in Chinese with English abstract)

Yang YH, Fan J, Hua Q, Gao J, Wang CL, Zhou L and Zhao T (2017) Inversion for the focal mechanisms of the 2017 Jiuzhaigou M7.0 earthquake sequence using near-field full waveforms. Chin J Geophys **60**: 4098–4104 (in Chinese with English abstract)

Yi GX, Long F, Liang MJ, Zhang HP, Zhao M, Ye YQ, Zhang ZW, Qi YP, Wang SW, Gong Y, Qiao HZ, Wang Z, Qiu GL and Su JR (2017) Focal mechanism solutions and seismogenic structure of the 8 August 2017 M7.0 Jiuzhaigou earthquake and its aftershocks, northern Sichuan. Chin J Geophys **60**: 4083–4097 (in Chinese with English abstract)

Zhang PZ, Shen Z, Wang M, Gan WJ, Burgmann R and Molnar P

(2004) Continuous deformation of the Tibetan Plateau from global positioning system data. Geology **32**: 809–812

Zhao C, Chen Z, Hua W, Wang Q, Li Z and Zheng S (2011) Study on source parameters of small to moderate earthquakes in the main seismic active regions, China mainland. Chin J Geophys **54**(6): 1478–1489 (in Chinese with English abstract)

Zhao G, Unsworth MJ, Zhan Y, Wang L, Chen X, Jones AG, Tang J, Xiao Q, Wang J, Cai J, Li T, Wang Y and Zhang J (2012) Crustal structure and rheology of the Longmenshan and Wenchuan M_W7.9 earthquake epicentral area from magnetotelluric data. Geology **40**: 1139–1142

Zhao LF and Xie XB (2016) Strong Lg-wave attenuation in the Middle East continental collision orogenic belt. Tectonophysics **674**: 135–146

Zhao LF, Xie XB, Wang WM, Zhang JH and Yao ZX (2010) Seismic Lg-wave *Q* tomography in and around Northeast China. J Geophys Res **115**: B08307

Zhao LF, Xie XB, Wang WM, Zhang JH and Yao ZX (2013a) Crustal Lg attenuation within the North China Craton and its surrounding regions. Geophys J Int **195**: 513–531

Zhao LF, Xie XB, He JK, Tian XB and Yao ZX (2013b) Crustal flow pattern beneath the Tibetan Plateau constrained by regional Lg-wave *Q* tomography. Earth Planet Sci Lett **383**: 113–122

Zheng XF, Yao ZX, Liang JH and Zheng J (2010) The role played and opportunities provided by IGP DMC of China National Seismic Network in Wenchuan earthquake disaster relief and researches. Bull Seismol Soc Amer **100**: 2866–2872